

## Tunable microlens actuated via a thermoelectrically driven liquid heat engine

Alireza Ousati Ashtiani and Hongrui Jiang

Citation: *Journal of Applied Physics* **115**, 243103 (2014); doi: 10.1063/1.4885879

View online: <http://dx.doi.org/10.1063/1.4885879>

View Table of Contents: <http://scitation.aip.org/content/aip/journal/jap/115/24?ver=pdfcov>

Published by the [AIP Publishing](#)

---

### Articles you may be interested in

[Thermally actuated tunable liquid microlens with sub-second response time](#)

*Appl. Phys. Lett.* **103**, 111101 (2013); 10.1063/1.4820772

[Electrowetting-driven variable-focus microlens on flexible surfaces](#)

*Appl. Phys. Lett.* **100**, 231105 (2012); 10.1063/1.4726038

[Microfluidic refractive-index sensors based on small-hole microstructured optical fiber Bragg gratings](#)

*Appl. Phys. Lett.* **98**, 221109 (2011); 10.1063/1.3597623

[A versatile liquid-core/liquid-twin-cladding waveguide micro flow cell fabricated by rapid prototyping](#)

*Appl. Phys. Lett.* **95**, 163702 (2009); 10.1063/1.3249771

[A p H -tunable hydrogel microlens array with temperature-actuated light-switching capability](#)

*Appl. Phys. Lett.* **94**, 081111 (2009); 10.1063/1.3089689

---



**AIP** | Journal of Applied Physics

*Journal of Applied Physics* is pleased to announce **André Anders** as its new Editor-in-Chief

# Tunable microlens actuated via a thermoelectrically driven liquid heat engine

Alireza Ousati Ashtiani<sup>1</sup> and Hongrui Jiang<sup>1,2,3,4,a)</sup>

<sup>1</sup>*Department of Electrical and Computer Engineering, University of Wisconsin–Madison, Madison, Wisconsin 53706, USA*

<sup>2</sup>*Materials Science Program, University of Wisconsin–Madison, Madison, Wisconsin 53706, USA*

<sup>3</sup>*Department of Biomedical Engineering, University of Wisconsin–Madison, Madison, Wisconsin 53706, USA*

<sup>4</sup>*McPherson Eye Research Institute, University of Wisconsin–Madison, Madison, Wisconsin 53706, USA*

(Received 16 May 2014; accepted 18 June 2014; published online 30 June 2014)

We have developed a thermally actuated liquid microlens. An embedded thermoelectric element is used to actuate the liquid based heat engine. A closed-loop system is harnessed to drive and stabilize the temperature of the heat engine. Direct contact between the thermoelectric device and the water results in greatly improved, sub-second thermal rise time (0.8 s). The water based heat engine reacts to the variation in the temperature via expansion and contraction. In turn, the shape of a pinned water-oil meniscus at a lens aperture is deformed in response to the net volume change in the water, creating a tunable microlens. A method to fabricate microfluidic devices with relatively high thickness (250–750  $\mu\text{m}$ ) and large length-to-depth aspect ratio (280:1) was developed and used in the process. After fabrication and thermal calibration, optical characteristic of the microlens was assessed. Back focal length of the microlens was shown to vary continuously from  $-19.6$  mm to  $-6.5$  mm as the temperature increased from  $5^\circ\text{C}$  to  $35^\circ\text{C}$ . A thin film air was further introduced to insulate the heat engine from the substrate to protect the microlens area from the temperature fluctuation of the heat engine, thus preventing the change of the refractive indices and thermally induced aberrations. Wavefront aberration measurement was conducted. Surface profile of the microlens was mapped and found to have a conical shape. Both 3-dimensional and 1-dimensional thermal models for the device structure were developed and thermal simulation of the device was performed. © 2014 AIP Publishing LLC. [<http://dx.doi.org/10.1063/1.4885879>]

## I. INTRODUCTION

The advent of affordable miniaturized digital imaging devices affects many aspects of people's life. Nowadays, every mobile phone has a small camera with an image quality that rivals much more expensive cameras from a decade ago. Capsule endoscopy is becoming a reality with the aid of lower power CMOS, sensors, and microlenses.<sup>1</sup> Many modern gadgets, for example, wearable head mounts displays, are now equipped with tiny cameras that are fitted inside their frames.<sup>2</sup>

From the perspective of lens designer, such miniaturized cameras have been traditionally made with a voice coil motor to move the lens barrel and provide a variable image distance for the camera.<sup>3</sup> These cameras are inherently bulky, and in their basic design, they share the same focusing mechanism as their bigger counterparts that are used in, for instance, digital single lens reflex cameras. Thus, in order to decrease the size and power consumption and increase focusing speed of small cameras, liquid microlens alternatives have been proposed in the past decade with proven commercial success in niche applications like intra-oral cameras.<sup>4</sup> Furthermore, numerous examples of liquid microlenses over flexible and hemispherical shapes have also been exhibited.<sup>5</sup>

In focus tunable liquid lenses, various actuation mechanisms have been used,<sup>6–12</sup> including liquid gradient refractive index,<sup>13</sup> pneumatic,<sup>14</sup> plasmofluidic,<sup>15</sup> electrowetting,<sup>16,17</sup>

electroactive polymer mechanical pump,<sup>18</sup> piezoelectric bimorph actuators,<sup>19</sup> stimulus responsive hydrogel,<sup>20,21</sup> and dielectric liquid lens,<sup>22</sup> each having their own advantages. Among the other actuation mechanisms, thermally driven lenses inherit the simplicity of a thermal drive. Various resistive based, thermopneumatically driven tunable microlenses have been reported in recent years.<sup>23,24</sup> Most of the thermally driven liquid lenses rely on natural heat dissipation and thus there exists a room for improvement in their cooling characteristic in order to make them faster.

We recently reported a thermoelectric (TE) driven liquid microlens which relies on the thermal expansion and contraction of the water inside a chamber to drive the lens.<sup>25,26</sup> With the aid of a closed-loop driver and bi-directional heat pumping mechanism, our microlens showed sub-second thermal response time. In this paper, we present a comprehensive study about the microlens structure, fabrication steps, optical characteristic, and finally thermal behavior of the microlens.

## II. DEVICE STRUCTURE AND METHOD OF OPERATION

Figure 1 shows the cross section of the proposed design. A TE element is placed and sealed on top of a deionized (DI) water filled cavity that is made from poly(isobornyl acrylate) (poly-IBA). On top of the thermoelectric element, a heatsink is placed to dissipate the heat generated in the TE device. Beneath the TE device, a water filled poly-IBA cavity resides. This cavity is laid on top of a thin film of air and the whole structure stands on top of a glass slide. Furthermore,

<sup>a)</sup>Author to whom correspondence should be addressed. Electronic mail: hongrui@engr.wisc.edu



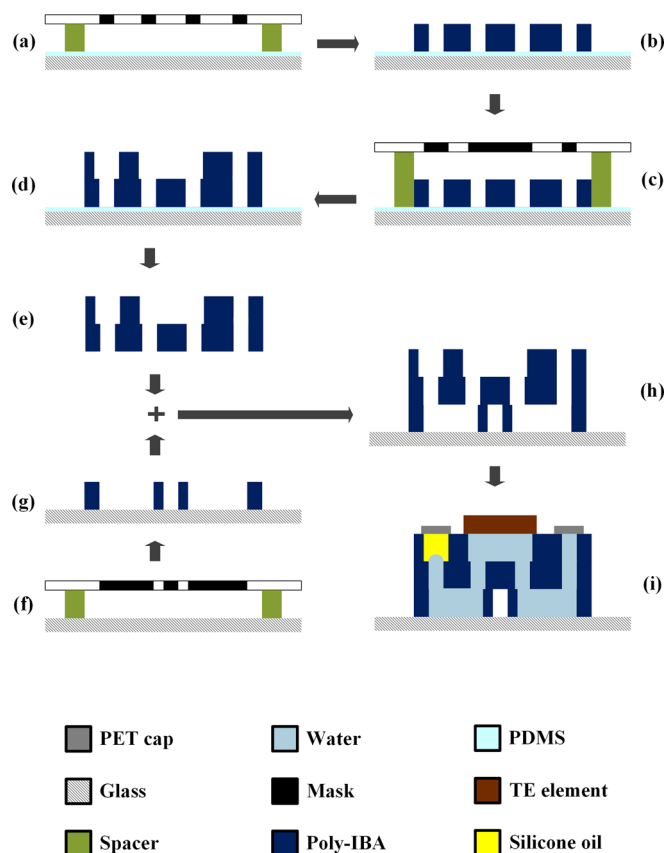


FIG. 2. (a) The mask for the first layer of the “structure-A” is put on top of the PDMS coated glass. The mask is spaced  $250\ \mu\text{m}$  above the substrate with the aid of liners and the inner spacing is filled with poly-IBA precursor. (b) After UV irradiation, the poly-IBA precursor is cross-linked and the layer that would make up the first layer of the “structure-A” is formed on top of the glass slide with a thickness of  $250\ \mu\text{m}$ . (c) The mask for second layer of the “structure-A” is put on top of the fabricated first poly-IBA layer. This mask is spaced  $500\ \mu\text{m}$  apart from the substrate via liners. (d) On top of the first poly-IBA layer, a second layer is formed that acts as a supporting structure in addition to forming the water and the oil cavity. (e) The bi-layer “structure-A” is peeled off from the PDMS coated substrate. It has a total thickness of  $500\ \mu\text{m}$ . The four small apertures have a diameter of  $1.5\ \text{mm}$  and the oil chamber has a diameter of  $5.5\ \text{mm}$ . (f) The mask for the bottom layer is laid on top of a glass slide. Spacing between the mask and the glass slide is held at  $250\ \mu\text{m}$  and the mask is supported by liners. (g) The poly-IBA layer that would make up water channels and provide mechanical support for the “structure-A” is formed on top of the glass slide. This structure is referred to as “structure-B.” (Small circular dimples provide mechanical support for the layer that will be placed on top of them later.) (h) The “structure-A” is laid on top of the “structure-B” and gaps between them are sealed with a thin layer of epoxy. (i) The TE element and the thermocouple sensor are laid on top of the device and sealed. After rinsing the device and filling the inner cavity of the device with water through the aperture on the right, the right aperture is closed with a PET cap. Finally, the oil chamber on the left is filled with silicone oil and a PET sealing cap is laid on top of the oil chamber.

are scattered onto the mask. Underneath them, extra liners are laid to fortify the mask (see Figure 2(a)). Subsequently, the void between the mask and the PDMS layer is filled with the poly-IBA precursor.<sup>21</sup> After filling the mask-to-glass gap with the poly-IBA precursor, the working piece is exposed to a collimated ultraviolet (UV) light source (OmniCure S2000, Lumen Dynamics Group Inc., Mississauga, ON, Canada) with a dosage of  $196\ \text{mJ cm}^{-2}$ . Since poly-IBA acts as a negative photoresist, radiated areas are cross-linked and form the structure. Once exposed, the mask is peeled away from

the glass and the residual poly-IBA precursor is washed away with ethanol, as shown in Figure 2(b). This first layer of the structure-A contains the holes for the microlens and the openings to pass the water from channels to the heat pump. In the next step and after rinsing and drying the working piece, another mask is laid on top of the structure, shown in Figure 2(c). Then, the void between the mask and the first layer of the structure-A is filled with the poly-IBA precursor and the next layer with the thickness of  $250\ \mu\text{m}$  is fabricated in a similar manner to the previous layer, giving a total thickness of  $500\ \mu\text{m}$ , as shown in Figure 2(d).  $500\ \mu\text{m}$  spacers are used in this step since the mask will be supported on the glass, while the spacing between the mask and the first layer should remain  $250\ \mu\text{m}$ . This second layer contains the oil chamber and the water heat pump cavity. Finally, the bi-layer structure-A is peeled from the PDMS coated glass with the aid of a scalpel, as it is shown in Figure 2(e). It is found that submerging the bi-layer structure into ethanol for tens of minutes facilitates the peeling step. During this process, visible poly-IBA volume change is observed. We attribute it to ethanol absorption into the poly-IBA network, which then tends to increase the volume and expand the polymer network. This results in a compressive stress that aids the release of the fabricated layer from the substrate.

In a similar process, a pair of water microchannels are fabricated on top of a 3 by 1 in. glass slide, as shown in Figures 2(f) and 2(g). In order to fabricate these channels, first a transparent and flexible mask is placed on top of the glass substrate, shown in Figure 2(f). The void between the mask and the glass is then filled with poly-IBA precursor. The transparent mask is separated from the glass via  $250\ \mu\text{m}$  liners. Next, it is exposed to a UV radiation of  $196\ \text{mJ cm}^{-2}$  to cross link the exposed areas of poly-IBA. This part of the device is called the “structure-B,” shown in Figure 2(g). With the aid of distributed spacers, a microfluidic layer with a relatively high thickness of  $250\ \mu\text{m}$  and length of  $60\ \text{mm}$  can be fabricated.

In the final step of the device structure fabrication, edges of the microchannels on the structure-B are wetted with an epoxy glue and then the structure-A is laid and pressed on top of it, as can be seen in Figure 2(h). The structure-B contains distributed dimples in order to support the structure-A on top. After 30 min, the epoxy glue is cured and microchannel is sealed. Without these dimples, dried poly-IBA could crack when pressed against the glass due to excessive bending at the sides. We opted to use dimples instead of covering the whole bottom area with the poly-IBA to provide extra thermal insulation. Most of the area on top of the glass slide of the structure-B is covered with air, which is a very good thermal insulator.

Device structure fabrication is followed by final device assembly. First, a type-T thermocouple sensor (Omega Engineering Inc., Stamford, CT, USA) is put onto a predefined recess and a small amount of thermally conductive epoxy (Arctic Alumina™, Arctic Silver Inc., Visalia, CA, USA) is applied on it. This thermocouple later touches the lower surface of the TE element and thus provides a temperature feedback for the device controller. After sensor placement, lower edges of the TE element (TE-65-0.6-0.8, TE

Technology, Inc., Traverse City, MI, USA) are coated with a thin layer of the epoxy glue and it is placed on top of the device structure, thus forming the final device assembly. Next, through the right hole of the microchannel, water is injected into the device which fills the heat pump cavity and then reaches the microlens opening. It was observed in our experiment that the wall of the opening is hydrophilic, unlike the upper surface of the poly-IBA, and the water is naturally sucked into the aperture and fills the opening and then pins at the upper edge of the left opening without the need of any further treatment. The contact angle of the poly-IBA surface is around  $92^\circ$  and thus water will not penetrate to the upper chamber to wet the surface of the poly-IBA. Hence, a water pinning boundary is formed at the upper edge of the opening due to the physical shape of the structure and the observed hydrophilicity of the walls of the poly-IBA. This edge at the opening pins the water and forms the microlens. After water filling, the upper chamber is filled with a silicone oil (DOW CORNING<sup>®</sup> 550 FLUID, Dow Corning Co., Midland, MI, USA). Since the refractive index of the silicone oil ( $n_{\text{oil}} = 1.4935$  at  $25^\circ\text{C}$ ) and the water ( $n_{\text{water}} = 1.3332$  at  $25^\circ\text{C}$ ) differs, the deformed water-oil interface refracts the light and acts as an optical microlens. Furthermore, since the liquid to liquid interface has minimal surface roughness,<sup>28</sup> the microlens surface profile remains optically smooth. After the oil filling, the upper layer is sealed. The finalized device is shown in Figure 2(i). Two different methods are used to seal the oil chamber. In one method, a glass slide is laid on top of the oil chamber and a small air bubble is intentionally left inside the oil chamber to compensate for the liquid volume change. In another method, a deformable membrane made from PET is then laid on top of the oil chamber to seal the microlens. This uppermost layer of the lens should be deformable or other means of volume change compensation should be provided in a sealed microlens design. Otherwise, a plausible mismatch in the thermal expansion coefficient of materials in the device structure and liquids will produce enough pressure to break structural parts of the device. This was manifested in some of our early experiments via breaking the microchannel sealing, which showed itself as a sudden leakage and the loss of the liquid. Finally, it is worth noting that the diameter of the deformable membrane is selected to be much bigger than the microlens aperture. Hence, when the liquid volume change deforms the membrane, the change in the membrane curvature is negligible compared to the change of the radius of curvature of oil-water meniscus and it does not affect the focal point of the microlens. The final fabricated device is shown in Figure 3.

#### IV. THERMAL MODELING

In order to gain more insight about the device behavior and so as to be able to optimize its characteristics, a model that closely represents the device is constructed. In the case of the proposed thermally actuated microlens, the most fundamental aspect of the whole system which governs its behavior would be its thermal system. The emphasis is mostly laid on the thermal heat engine. In this design, the thermal system of the microlens consists of a couple of major

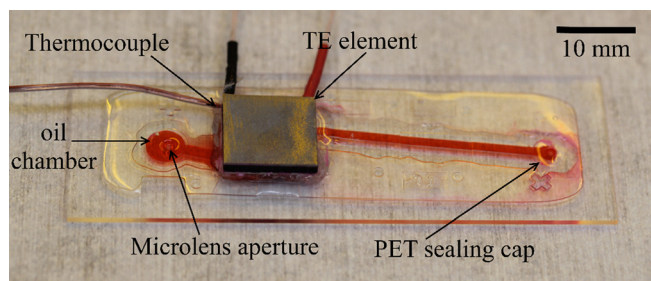


FIG. 3. The fabricated device structure. The heatsink on top of the TE element is removed and water inside the device is dyed for better clarity. The water meniscus opening is shown as the inner aperture on the left. This aperture would pin the water and form the microlens.

components. Based on the placement from bottom to top, the model comprises:

1. Glass substrate: the glass substrate used in the microlens acts as a thermal mass and also a heat radiator since it has a relatively large surface area, which will dissipate the heat through convection and radiation. While the device is set at different temperatures, the glass substrate would either absorb or release thermal energy towards the rest of the thermal system.
2. Air gap: An air gap improves the response time of the system and further insulates the heat pump from the surroundings, which will lead to reduced energy consumption. This air gap has a relatively large length to depth ratio (around 40) and the heat convection is negligible.<sup>29</sup> Furthermore, the heat capacitance of this air layer can be omitted since the mass of it is almost zero in our application, compared to the rest of the system. Thus, the air gaps would act as a simple resistive layer between the glass and the heat pump.
3. Poly-IBA: The whole body of the heat engine and the bulk of the microchannels that connects the heat engine to the microlens are made from poly-IBA. It possesses both low thermal conductivity ( $0.2 \text{ W m}^{-1} \text{ K}^{-1}$ ) and low specific heat ( $1.1 \text{ J g}^{-1} \text{ K}^{-1}$ ),<sup>30</sup> which makes it a good insulating material candidate.
4. Heat engine: At the center of the driving mechanism of the microlens, a liquid filled heat engine resides. The water that is encapsulated between the poly-IBA layer and the TE element would undergo a volume change in response to the temperature change and will drive the liquid meniscus that forms the microlens. The heat engine has a very high width to height ratio and on top, it is connected to a TE element which has an alumina layer with high thermal conductivity of  $20 \text{ W (m K)}^{-1}$  (As per information provided by the TE manufacturer). As will be shown later, lateral temperature gradient in the heat engine is minimal and it empowers us to use a simpler 1-dimensional (1D) thermal circuit model to further assess the dynamic behavior of the microlens in a closed-loop system.
5. TE element: On top of the water based heat engine, a thermoelectric element resides. The lower surface of the TE element is thermally shorted to the thermocouple. As a result, the thermocouple sensor provides a temperature feedback from the lowermost layer of the TE device. As

will be shown later, because of the high thermal conductivity of alumina, the lowermost layer of the TE element shows minimal temperature gradient and its temperature changes homogeneously in the whole bulk of the layer throughout the most of both transient and steady state conditions. It means that the temperature feedback from thermocouple represents the temperature of the whole bulk of the lowermost alumina surface of the TE element. Based on this, the TE element in conjunction to a thermocouple sensor and a proportional-integral-derivative (PID) controller provides a closed-loop temperature controlled source to drive the heat engine. One advantage of using a thermoelectric element to drive a thermal system comes from the fact that it can act as a bi-directional heat pump. This bi-directionality results in a faster lens since the cooling of the lens is not based on natural heat dissipation and the closed-loop system can be designed to operate with a slight overshoot, which in turn decreases rise time and fall time.

6. Heatsink: On top of the TE element, one Aluminum based heat sink is used to dissipate the generated heat. Thermal mass of the heatsink is larger than the other components. This big thermal mass in conjunction to the low thermal resistivity constitutes a low pass filter that, from the perspective of a thermal circuit, effectively grounds the thermal system and has positive effect on the stabilization of the thermal system.

A 3-dimensional (3D) model of the device was developed in ANSYS workbench software package to evaluate both transient and steady-state thermal response. Figure 4 shows the steady state temperature response to a DC input voltage of 280 mV. As can be seen in Figure 4(a), visible temperature gradient occurs mostly around the thermal engine area. Furthermore, due to the thin air film, there is only a negligible temperature fluctuation across the optical parts of the device. It was found that for a steady state water temperature of 15 °C, the temperature around the microlens aperture changes by only  $-0.8$  °C with regard to the ambient temperature of 22 °C, compared to  $-1.2$  °C in an embodiment without the thin air film, which shows a 34% of improvement. It is important to keep the temperature fluctuation minimal at the water meniscus since the refractive index is a function of the temperature and any temperature variation in the microlens will result in increased and uncontrolled aberration. In addition, with regard to the normal plane of the device (any plane parallel to the glass substrate), the tangential component of the temperature gradient is minimal as shown in Figures 4(b)–4(d) and the heat engine mostly has a normal temperature gradient. As a consequence, the temperature gradient can be adequately represented by a 1D thermal model, which confirms our initial assumption of the applicability of a 1D thermal model. Based on this, a lumped capacitance Cauer-network thermal circuit was developed as can be seen in Figure 5. This model uses various lumped capacitance and resistance values for the materials that are used in the device. In order to have a complete, thermal-electrical circuit, thermoelectric parameters need to be added to the thermal circuit. The thermal and electrical domains

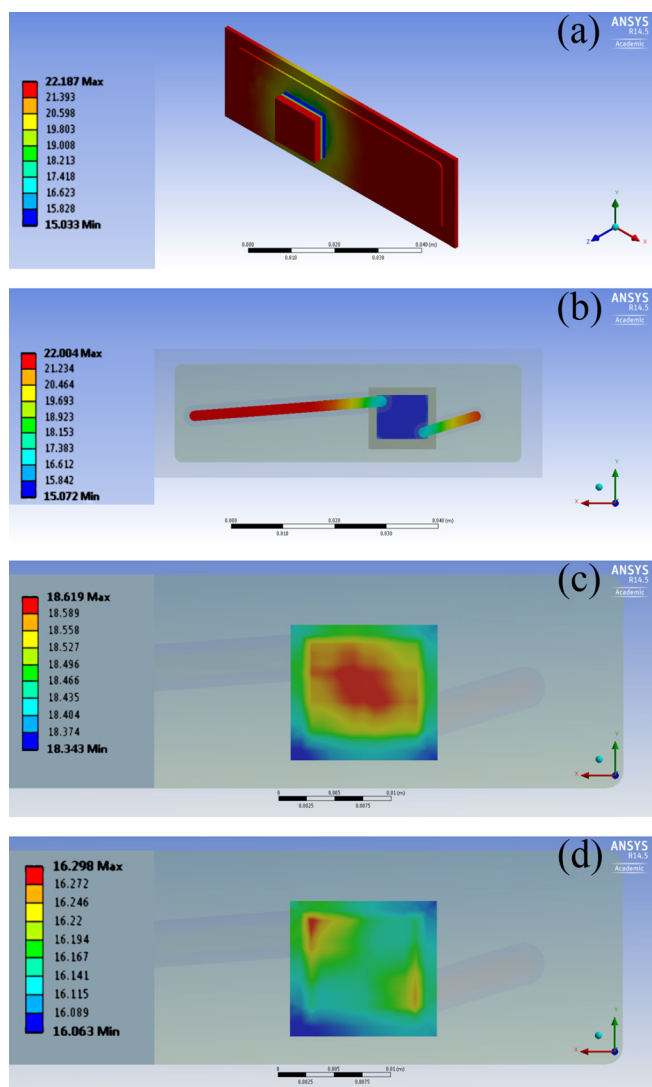


FIG. 4. (a) Temperature distribution in the device structure. Steady state temperature in the water chamber is 15 °C. (b) Temperature distribution in the water filled regions of the device in steady state condition for the same device. Note that the temperature gradient around the microlens aperture area in the microchannel is minimal and almost negligible. This prevents refractive index fluctuations due to the temperature change of the heat engine. (c) Temperature distribution in the mid water plane after 3000 ms. As can be seen, temperature is almost constant across the whole area. (d) Temperature distribution in the mid water plane after 8300 ms at steady state condition. Difference between maximum and minimum temperature is around 0.2 °C.

interact through a dependent voltage source as shown in Figure 5. Parameters and methods of modelling are thoroughly described elsewhere.<sup>31</sup> Centered on this thermal-electrical circuit, a SIMULINK model in MATLAB was developed to simulate various response of the thermal system. In Figure 6, the impulse function response of the system is shown and compared with the ANSYS results. As can be seen, the impulse function response of the 1D model closely follows the result of the ANSYS transient thermal-electrical simulation. In order to further validate the 1D model, the closed-loop system behavior was assessed in the 1D model and compared with the measured data. Results of the measured temperatures in comparison to the simulated data will be presented in Sec. V.

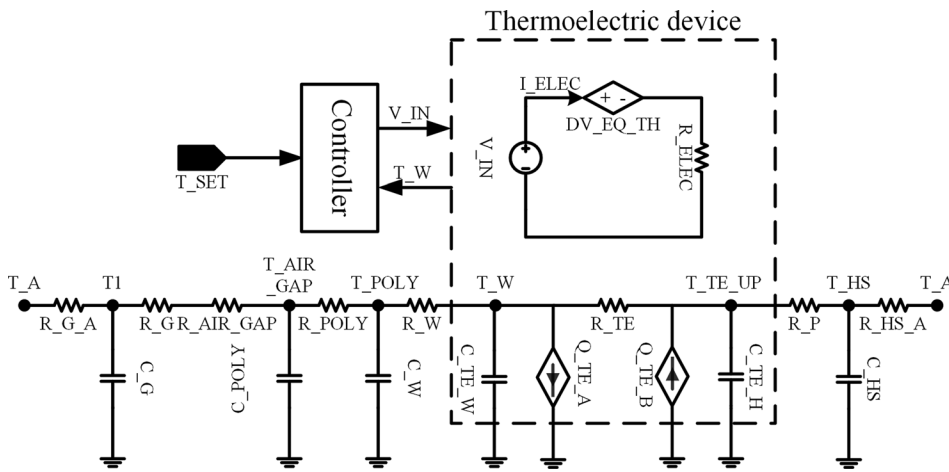


FIG. 5. The thermal-electrical equivalent circuit of the system. Abbreviations used are as follows: R: Resistor. C: Capacitor. G\_A: Glass to ambient. G: Glass. W: Water. TE: Thermoelectric device. P: Thermal paste. HS: Heatsink. T\_SET: Setpoint temperature. T\_A: Ambient temperature. T\_W: The temperature of lower TE plate which is in touch with the water. ELEC: Electrical. DV\_EQ\_TH: Equivalent voltage of the TE element. Q\_TE\_A: Absorbed heat at the lower TE plate. Q\_TE\_B: Injected heat at the upper TE plate. The controller senses T\_W and supplies V\_IN to the Thermoelectric device in order to stabilize T\_W at T\_SET.

**V. CLOSED-LOOP EXPERIMENTAL RESULTS**

A closed-loop feedback system was used to drive the TE device. The temperature feedback was provided to a PID controller (ATEC302NBM, Accuthermo Technology Corp., Fremont, CA, USA) via a type-T thermocouple junction (Accuthermo Technology Corp., Fremont, CA, USA). The microlens was placed on top of various images and the optical functioning of the lens was observed via a CCD equipped stereoscope (MSZ-1500, Nikon Instruments Inc., Melville, NY, USA), while the time domain thermal response of the device was logged via a software interface provided for the controller. In order to observe the change in the optical characteristic as a function of the temperature, the temperature was varied from 20 °C to 30 °C and vice versa. A median temperature of 25 °C was chosen because it is close to room temperature; therefore, the heat engine in its resting position would only need a fraction of energy compared to extremum temperatures.

After the system assembly and automatic calibration of the controller, a response time shown in Figure 7 was obtained. During the experiment, maximum supplied voltage on the TE remained under 6 V and in the steady state, it stayed around 2.8 V which is very low compared to, for example, electrowetting-based microlenses. With regard to Figure 7 and by examining the rising edge of the measured

temperature signal, a thermal rise time of 0.8 s was observed for the device while going from 20 °C to 30 °C. This response time was defined as the time needed for the temperature difference to change from 10% to 90% of its final value of 10 °C. Likewise, the fall time was measured to be 1.4 s (not shown). As shown in Figure 7, the simulated and measured thermal response time show similar behaviour of a second order PID governed system, which further validates the 1D thermal-electrical circuit. During the experiment as anticipated, the water temperature change ultimately resulted in a variation of focal length, which was clearly evidenced by image modification compared to the initial condition, which can be seen in Figure 8.

**VI. OPTICAL MEASUREMENT AND CHARACTERISTICS**

**A. Focal length measurement**

One of the key characteristics of any lens is the focal length. In order to measure the focal length of a microlens, various methods have been proposed and used such as holographic microscopy,<sup>32</sup> Mach-Zehnder interferometry,<sup>33</sup> and combined Twyman-Green and Mach-Zehnder interferometry.<sup>34</sup> Most of the methods used to find focal spot of a microlens, however, need relatively sophisticated optical setup and

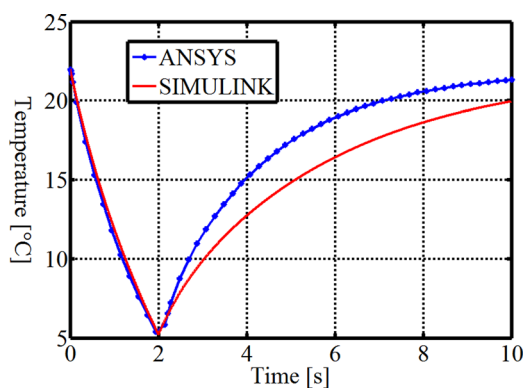


FIG. 6. Impulse response of a 3D thermal-electrical multiphysics model solved in ANSYS compared to the 1D circuit model developed in MATLAB SIMULINK. An impulse with a magnitude of 2V and duration of 2s is applied to the system to assess transient responses of both models.

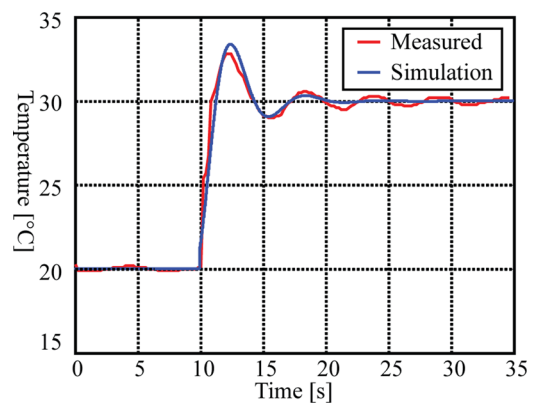


FIG. 7. The thermal-circuit-based simulated and the experimental time-domain step function thermal response of the device. A step function of 30 °C (an increment of 10 °C) is applied at the time instant of 10 s to the system.



FIG. 8. Captured images through a microscope and the microlens. (a) An initial image at 20 °C. (b) An image from the same object at 25 °C. (c) The image at 30 °C. As can be seen here, by increasing the temperature, microlens becomes more diverging and the resulting image becomes smaller.

a simple method that results in a measurement with adequate accuracy is needed. In our previous works, we used an image tracking optical table apparatus to find the focused image of a collimated and expanded HeNe (633 nm) single mode Gaussian laser beam to spot the focal point. In this method, the said light source illuminates the lens and then a CCD sensor on a linear translational stage is moved on the optical axis of the lens to find the point, wherein the focused spot of the lens has the minimal diameter. Because of spherical aberration, the resulting spot does not resemble a diffraction limited airy disk. Instead, it becomes a larger circular image and the axial position that corresponds to the circle of the least confusion is used as the reference in which the focal point is measured. After finding said position, the distance between the lens and the CCD imager is measured which equals the focal length. There is, however, a fundamental problem in this method which limits its functionality to the measurement of the lenses with positive focal lengths. In a lens with a negative focal length, the image distance of a collimated light source will become negative resulting in a virtual image and thus it cannot project a focused point image on the CCD. In order to circumvent this issue, a plano convex auxiliary lens with an aperture diameter of 25 mm and a focal length of +100 mm is added between the lens and the CCD imager. Then in a similar method as above, the distance of the circle of least confusion is measured from the auxiliary lens and later, based on lensmaker's equation, the position of the virtual image is calculated which results in an indirectly measured focal point. This method works satisfactorily yet it gives rise to an additional source of error from the auxiliary lens itself. For example, in our setup, the tolerance mentioned by the manufacturer for the focal point of the auxiliary lens is 2%, which results in a  $\pm 2$  mm deviation in the focal length measurement. In addition, based on lens specification provided by manufacturer, chromatic aberration adds +0.7 mm of shift in the focal length. Furthermore, in the commonly used translational stage, it is hard to find the distance between the origin on the translational stage and the placement of the optical object that sits on it. This adds an extra measurement error in assessing various distances on the optical setup. Based on our previous experiment, we know that this microlens has a focal length range of approximately just a couple of mm up to a couple of tens of millimeter. Thus, even without considering aberration, it is conceivable to see that various errors are added up and cumulative error becomes comparable to the focal length of the microlens itself.

In order to address the aforementioned issues, an improved, simpler and direct focal length measurement apparatus is designed as shown in Figure 9. From left to right, this setup consists of a collimated light source, a reference

translational stage with a latch to clip various optical objects onto it, a plano concave lens with  $f = 100 \pm 2$  mm focal length and 25 mm diameter which sits roughly at twice its focal length from the optical object, and finally a CCD imager that is positioned at around twice focal length of the auxiliary lens from the auxiliary lens. The collimated light source can be thought of as an infinitely far object for the apparatus, and the optical object that sits on the reference translational stage can be considered a light modulator that creates an intermediate object, which will be reproduced after passing through the lens onto the CCD imager.

In order to set up the apparatus, the first step consists of fine tuning the apparatus. Initially, an image printed on a thin transparent film is positioned on the reference translational stage, which is fixed at the origin. Then, the collimated light produces an intermediate object which is the light that is modulated by the thin film. Next, by slightly moving the auxiliary lens and the CCD imager, the position wherein the sharpest image is formed on the CCD imager is found. Finally, the position of the auxiliary lens and the CCD imager is fixed and the apparatus is now calibrated. In other words, the optical setup now projects the object that sits on the origin of the reference translational stage (that we called the intermediated object) to a focused image on the CCD.

This apparatus can be used now to accurately measure the focal point of a given microlens. In the first step, the lens is placed on the reference translational stage and replaces the transparent film. Next, the collimated light source illuminates the microlens and forms an intermediate object which is the circle of least confusion. This intermediate object forms at a position that is anywhere in mm range from the microlens since the range of the focal length of the investigated

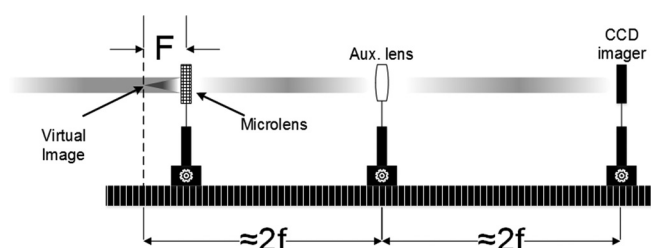


FIG. 9. Focal length measurement setup. It consists of three translational stages on top of a precision optical rail. A collimated light source from the left illuminates the microlens that is placed on the first stage, i.e., the reference translational stage. The focused image of the collimated beam after passing through the microlens will act as an object for the auxiliary lens, which in turn projects it onto the CCD sensor. By fine tuning the reference translational stage, the place of the projected image of the microlens will align with the calibrated origin of the setup. The distance traveled by said translational stage "F" equals the additive inverse of the focal length of the microlens.

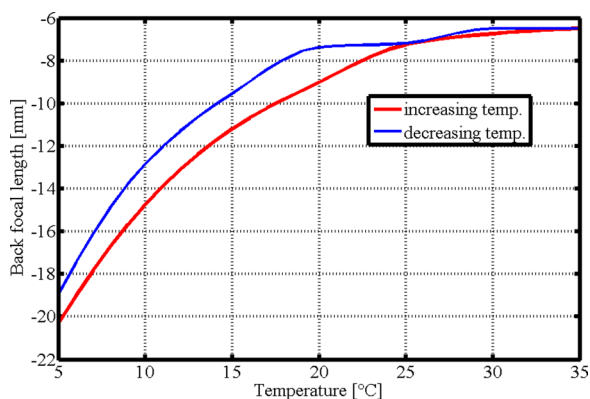


FIG. 10. The back focal length of a sample of microlens as a function of temperature. The back focal length has negative values since the microlens has a convex water-into-the-oil meniscus shape, which forms a diverging microlens. The microlens shows a slight hysteresis, similar to electrowetting and some other liquid microlenses.

microlens is anticipated to be a couple of mm to tens of mm. This intermediate object would act as a newly formed optical object for the auxiliary lens. Now the reference translational stage is moved until the circle of the least confusion is reproduced on the CCD imager. When the sharpest image with the smallest circle of confusion is found on the CCD imager, the relative movement of the reference translational stage compared to the origin point is measured. Because the initial object is a collimated light source, the position of the intermediate object after passing through the microlens represents the focal point of the microlens. Thus, the measured distance stands for the additive inverse of the focal length of the microlens as the reference translational stage is relocated to a point to compensate for the movement of the intermediate object. Hence with this apparatus, we are able to accurately measure both positive and negative focal length of the microlens and errors will be limited only to the measurement accuracy of the optical table and translational stage.

With the aid of the aforementioned setup, the back focal length of the microlens was measured while the temperature was changed from 5 °C to 35 °C. Measurement of the back focal length is more meaningful in this experiment since it is hard to spot the exact position of the principal planes of the

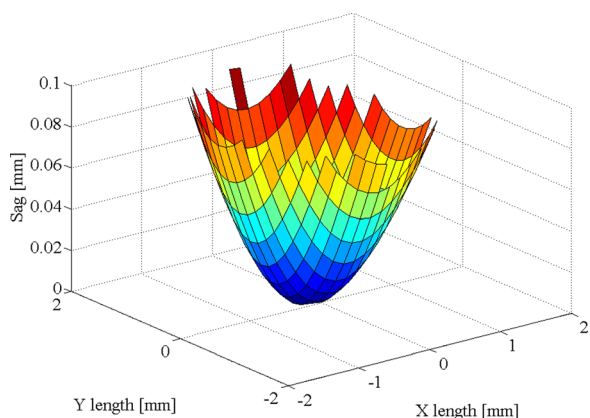


FIG. 11. Microlens sag. Sag is calculated from the wavefront aberration data that are extracted from a Shack-Hartmann sensor. The result is from a sample microlens at a temperature of 22 °C and a back focal length of -8.1 mm.

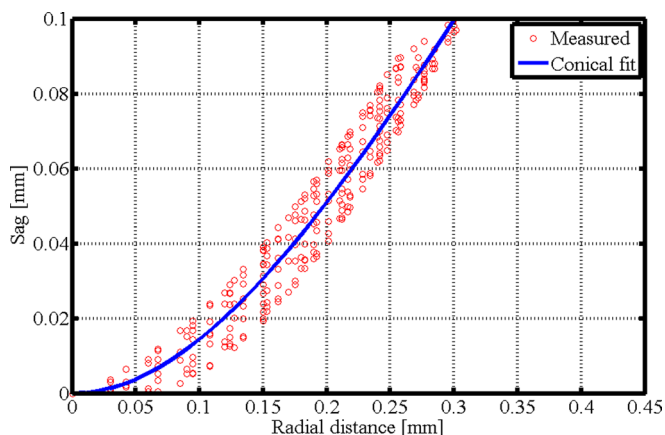


FIG. 12. Microlens surface profile (sag) as a function of the radial distance from the optical axis. The result is from a sample microlens at a temperature of 22 °C and a back focal length of -8.1 mm.

microlens. Thus, it is more suitable to define the distance of the focal spot from the outermost surface of the glass substrate, and hence the back focal length is measured. The experiment was conducted in both increasing temperature and decreasing temperature. The results are shown in Figure 10. As it can be seen, the lens showed a small amount of hysteresis, comparable to hysteresis shown in electrowetting.<sup>35</sup> We believe that this hysteresis is due to advancing and receding contact angle hysteresis at the pinning edge of the water-oil meniscus. The microlens showed a back focal lens from -19.6 to -6.5 mm. In the sample tested, the water meniscus had a convex shape and bulged into the oil chamber. As a result, the microlens became a diverging lens.

**B. Surface profile and aberration measurement**

In practical application, it is constructive to measure the aberration of the microlens. A Shack-Hartmann wave-front sensor (WFS150C, Thorlabs Inc., Newton, NJ, USA) was used to extract the wavefront profile of a collimated light source after passing through the microlens. In the setup used, a HeNe light source was used. Light source from the laser is a Gaussian beam and thus care was taken to put the lens well within the Rayleigh length of the laser source. Similar to methods mentioned in earlier works from our group,<sup>36,37</sup> the wavefront data measurement was used to construct the surface profile of a sample microlens at a temperature of 22 °C and a focal length of -8.1 mm. The resulting microlens profile is shown in Figure 11. In addition to compiling the microlens surface profile, calculated microlens sag can be used to gain more insight about the microlens shape. Based on the surface profile data, a curve fitting code developed in MATLAB was used to fit the surface profile into a conical

TABLE I. Microlens surface profile fitting parameters.

Parameter	Conical fit	4th aspheric fit
$C$ (curvature) [ $\text{mm}^{-1}$ ]	3.0221	2.93
$K$ (conic constant)	-3.4322	-2.322
$A_4$ (4th order aspheric term) [ $\text{mm}^{-3}$ ]	N/A	-1.285
$RMSE$ (root mean square of error) [ $\mu\text{m}$ ]	6.51	6.48

TABLE II. Wavefront aberration in terms of Zernike polynomials.

Index	Traditional name	Coefficient (wave)
1	Piston	6.890995261
2	X-Tilt	0.241706161
3	Y-Tilt	-0.309636651
4	Astigmatism	-0.060031596
5	Defocus	-6.966824645
6	Astigmatism	0.060031596
7	Trifoil	-0.083728278
8	Coma	0.197472354
9	Coma	-0.344391785
10	Trifoil	0.039494471
11	Tetrafoil	0.055292259
12	Secondary astigmatism	-0.009478673
13	Primary spherical	0.312796209
14	Secondary astigmatism	-0.085308057
15	Tetrafoil	0.058451817

shape and a 4th order aspheric shape. In this calculation, the microlens sag was fitted by the generalized aspheric lens equations. Aspheric surface profiles have been traditionally defined with the following equation:

$$Z(s) = \frac{Cs^2}{1 + \sqrt{1 - (1+k)C^2s^2}} + A_4s^4 + \dots, \quad (1)$$

whereas  $Z$  represents sag,  $C$  the radial distance from the optical axis,  $K$  the conic constant,  $A_4$  the 4th order aspheric term, and higher orders are truncated here. The scatter plot and the best fitted curve for a conical surface profile are shown in Figure 12. As shown, the microlens has a spherical surface at the center and towards the edges, it becomes linearly shaped. Results of the curve fitting parameters are tabulated in Table I. In one scenario, the conic lens (no aspheric terms) is used and in the other, 4th order aspheric term is added to demonstrate any positive effect on finding a better fitting and reducing the root mean square of error of the fitted curve. As shown in Table I, the conical profile suffices and there is no valuable error reduction by adding the 4th order aspheric term. In addition, as can be seen in Table I, in either case the surface profile is hyperbolic. It is anticipated since the water-oil interface is pinned at the edges of the aperture and thus the closer to the edges, the more linearly shaped surface profile we will see.

Finally, the wavefront aberration is represented in Table II, in terms of Zernike polynomials. From Table II, we can see that the microlens has a spherical aberration of 0.312 wavelength.

## VII. CONCLUSION

A thermally actuated, thermoelectrically driven liquid microlens was developed. Integration of the thermoelectric device into the liquid chamber resulted in more responsive microlens. Segregation of the heat engine liquid chamber and the substrate resulted in reducing the temperature fluctuation on the optical parts of the microlens device. A 3D model was developed to assess the thermal behavior of the device. Based on the 3D model results, validity of using a

1D model was checked and a lumped capacitance thermal circuit for the device was developed.

From optical standpoint, an improved focal length measurement set-up was used to measure the focal point of the microlens. A closed-loop system was harnessed to drive the microlens at various temperatures and the resulting back focal length was measured. Microlens aberration was measured with a Shack-Hartmann wave-front sensor. The surface profile of the lens was deduced and found to be a conical surface.

A practical microfluidic fabrication method was also developed. The method proposed here can similarly be used in fabricating other microfluidic systems. Compared to other omnipresent manufacturing methods, for instance, the use of SU-8 photoresist to realize a microfluidics device, the proposed method provides a simple way to make a device with relatively high (250–750  $\mu\text{m}$ ) thickness and at the same time very high length to thickness ratios (280:1 in our case).

In future works, the device packaging and sealing will be improved to reduce gradual water evaporation. Furthermore, the same driving mechanism will be used to actuate an array of microlenses and different aperture sizes. In addition, reducing the thermal budget of the microlens is needed to increase the speed and reduce the energy consumption of the microlens, thus opening the door for practical applications of the thermally driven liquid microlenses. Based on this, emphasis will be put on reducing the size of the liquid chamber and the whole thermal engine. The use of liquids with higher thermal expansion is considered as an option to increase the effect of the liquid thermal expansion on the tunability of the microlens. With additional improvement, the thermoelectrically driven microlens will be tailored to meet demands of various applications that need tunable liquid microlenses, in a relatively simple package.

## ACKNOWLEDGMENTS

This work was supported by the U.S. National Science Foundation under Grant No. ECCS 0745000. The authors would like to thank Dr. B. Aldalali, A. Kanhere, and Dr. C. H. Li for discussion and help.

<sup>1</sup>A. Moglia, A. Menciassi, M. Oliver Schurr, and P. Dario, *Biomed. Microdevices* **9**, 235 (2007).

<sup>2</sup>J. Rolland and H. Fuchs, *Presence: Teleoperators Virtual Environ.* **9**, 287 (2000).

<sup>3</sup>H. C. Yu, T. Y. Lee, S. J. Wang, M. L. Lai, J. J. Ju, D. R. Huang, and S. K. Lin, *IEEE Trans. Magn.* **41**, 3979 (2005).

<sup>4</sup>K. Kagawa, H. Tanabe, C. Ogata, Y. Ogura, Y. Nakao, T. Toyoda, Y. Masaki, M. Ueda, and J. Tanida, *Jpn. J. Appl. Phys.* **48**, 09LB04 (2009).

<sup>5</sup>D. Zhu, X. Zeng, C. Li, and H. Jiang, *J. Microelectromech. Syst.* **20**, 389 (2011).

<sup>6</sup>Y. C. Seow, S. P. Lim, and H. P. Lee, *Lab Chip* **12**, 3810 (2012).

<sup>7</sup>J. Chen, W. Wang, J. Fang, and K. Varahramyan, *J. Micromech. Microeng.* **14**, 675 (2004).

<sup>8</sup>K. S. Hong, J. Wang, A. Sharonov, D. Chandra, J. Aizenberg, and S. Yang, *J. Micromech. Microeng.* **16**, 1660 (2006).

<sup>9</sup>N. T. Nguyen, *Biomicrofluidics* **4**, 031501 (2010).

<sup>10</sup>X. Mao, S. C. S. Lin, C. Dong, and T. J. Huang, *Lab Chip* **9**, 1583 (2009).

<sup>11</sup>Y. Zhao, Z. S. Stratton, F. Guo, M. L. Lapsley, C. Y. Chan, S. C. S. Lin, and T. J. Huang, *Lab Chip* **13**, 17 (2013).

<sup>12</sup>L. Pang, H. M. Chen, L. M. Freeman, and Y. Fainman, *Lab Chip* **12**, 3543 (2012).

- <sup>13</sup>H. Huang, X. Mao, S. C. S. Lin, B. Kiraly, Y. Huang, and T. J. Huang, *Lab Chip* **10**, 2387 (2010).
- <sup>14</sup>P. Fei, Z. He, C. Zheng, Y. Men, and Y. Huang, *Lab Chip* **11**, 2835 (2011).
- <sup>15</sup>C. Zhao, Y. Liu, Y. Zhao, N. Fang, and T. J. Huang, *Nat. Commun.* **4**, 2305 (2013).
- <sup>16</sup>B. Berge, in *Proceedings of IEEE International Conference on Microelectromechanical Systems* (2005), p. 227.
- <sup>17</sup>F. Krogmann, W. Mönch, and H. Zappe, *J. Microelectromech. Syst.* **17**, 1501 (2008).
- <sup>18</sup>S. T. Choi, J. Y. Lee, J. O. Kwon, S. Lee, and W. Kim, in *SPIE MOEMS-MEMS: Micro- and Nanofabrication* (2009), p. 72080-9.
- <sup>19</sup>T. Kaneko, T. Ohmi, N. Ohya, N. Kawahara, and T. Hattori, in *Proceedings of International Solid State Sensors and Actuators Conference Transducers* (1997), Vol. 1, p. 63.
- <sup>20</sup>L. Dong, A. K. Agarwal, D. J. Beebe, and H. Jiang, *Nature* **442**, 551 (2006).
- <sup>21</sup>L. Dong, A. K. Agarwal, D. J. Beebe, and H. Jiang, *Adv. Mater.* **19**, 401 (2007).
- <sup>22</sup>Y. S. Lu, H. Tu, Y. Xu, and H. Jiang, *Appl. Phys. Lett.* **103**, 261113 (2013).
- <sup>23</sup>A. Werber and H. Zappe, *J. Microelectromech. Syst.* **17**, 1218 (2008).
- <sup>24</sup>J. K. Lee, K. Park, G. Lim, H. Kim, and S. H. Kong, *J. Opt. Soc. Korea* **16**, 22 (2012).
- <sup>25</sup>A. O. Ashtiani and H. Jiang, *Appl. Phys. Lett.* **103**, 111101 (2013).
- <sup>26</sup>A. O. Ashtiani and H. Jiang, in *Proceedings of 2013 Transducers & Eurosensors XXVII: The 17th International Conference on Solid-State Sensors, Actuators and Microsystems* (2013), p. 2604.
- <sup>27</sup>L. Dong and H. Jiang, *Appl. Phys. Lett.* **91**, 041109 (2007).
- <sup>28</sup>F. Krogmann, W. Mönch, and H. Zappe, *J. Opt. A: Pure Appl. Opt.* **8**, S330 (2006).
- <sup>29</sup>K. Hollands, T. Unny, G. Raithby, and L. Konicek, *ASME J. Heat Transfer* **98**, 189 (1976).
- <sup>30</sup>M. Kok, K. Dem, and Y. Aydogdu, *Int. J. Sci. Technol.* **3**, 37 (2008).
- <sup>31</sup>J. A. Chavez, J. A. Ortega, J. Salazar, A. Twb, M. J. Garcia, S. S. Group, and U. P. De Catalunya, in *Proceedings of IEEE Instrumentation and Measurement Technology Conference* (2000), Vol. 2, p. 1019.
- <sup>32</sup>F. Charrière, J. Kühn, T. Colomb, F. Montfort, E. Cuche, Y. Emery, K. Weible, M. Marquet, and C. Depeursinge, *Appl. Opt.* **45**, 829 (2006).
- <sup>33</sup>T. Miyashita, M. Kato, and J. Ohta, *Opt. Eng.* **48**, 73609 (2009).
- <sup>34</sup>S. Reichelt and H. Zappe, *Appl. Opt.* **44**, 5786 (2005).
- <sup>35</sup>F. Li and F. Mugele, *Appl. Phys. Lett.* **92**, 244108 (2008).
- <sup>36</sup>C. Li, G. Hall, X. Zeng, D. Zhu, K. Eliceiri, and H. Jiang, *Appl. Phys. Lett.* **98**, 171104 (2011).
- <sup>37</sup>C. Li, G. Hall, D. Zhu, H. Li, K. Eliceiri, and H. Jiang, *J. Microelectromech. Syst.* **21**, 530 (2012).